Journal of Molecular Spectroscopy 378 (2021) 111458

Contents lists available at ScienceDirect

Journal of Molecular Spectroscopy

journal homepage: www.elsevier.com/locate/jms

Mid-infrared spectroscopic signatures of dibenzopyrene cations – The effect of symmetry on PAH IR spectroscopy

Jordy Bouwman [a,*], Harold Linnartz [a], Alexander G.G.M. Tielens [b]

[a] Laboratory for Astrophysics, Leiden Observatory, Leiden University, PO Box 9513, 2300 RA Leiden, the Netherlands
[b] Leiden Observatory, Leiden University, PO Box 9513, 2300 RA Leiden, the Netherlands

ARTICLE INFO

Article history:
Received 24 November 2020
Accepted 29 March 2021
Available online 15 April 2021

Keywords:
Mid-IR spectroscopy
Interstellar medium
Polycyclic aromatic hydrocarbons
Quadrupole ion trap
Mass spectrometry

ABSTRACT

In this work, we characterize – for the first time – in the gas phase infrared spectra of three isomeric Polycyclic Aromatic Hydrocarbon (PAH) cations of $C_{24}H_{14}$ composition that belong to distinctly different symmetry groups (C_{2h}, C_s and C_1). Mid-infrared (Mid-IR) spectra are recorded by means of infrared multiple photon dissociation (IRMPD) spectroscopy at the free electron laser for infrared experiments (FELIX) laboratory. The measured infrared (IR) band positions compare reasonably well with density functional theory (DFT) calculated values. The number of IR active bands increases as the symmetry of the molecule lowers. The IRMPD spectra of irregular PAHs are found to be dense and do not resemble the sharp signatures typical of astronomical IR bands, but rather look like the broad plateau on which these are perched. This lends credit to the GrandPAH hypothesis that suggests that small and irregular PAHs are weeded out by the strong interstellar radiation field and only large regular PAHs remain.
© 2021 The Authors. Published by Elsevier Inc. This is an open access article under the CC BY license (http://creativecommons.org/licenses/by/4.0/).

1. Introduction

Interstellar IR emission bands observed at wavelengths of 3.3, 6.2, 7.7, 8.6 and 11.2 μm are seen towards a variety of astronomical objects [1,2]. Photodissociation regions, planetary nebulae, reflection nebulae, and even entire galaxies are set aglow by the omnipresent IR emission features [3]. It has now widely been accepted that the IR emission stems from large free-floating PAHs (typically $N_C > 50$) that – after being excited by a (vacuum) ultraviolet (UV) photon – relax back to the ground state by emitting a cascade of mid-IR photons [4].

Schlemmer et al. [5] were the first to confirm that UV excitation of PAHs is indeed the driving force for the appearance of the interstellar IR bands. To achieve this, they conducted very sophisticated laboratory measurements that allowed for sensitive frequency resolved detection of the IR light emanating from laser excited neutral PAHs. Based on IR emission measurements of a number of small neutral PAHs, including a few methyl- and hetero atom substituted species, Schlemmer and coworkers concluded that small neutral PAHs can at most be minor contributors to the IR emission bands and that large PAHs and PAH cations are likely more relevant contributors [6,7]. They furthermore suggested that experimentally obtained absorption spectroscopic data and DFT computed spectra can serve as a good starting point to simulate interstellar PAH emission profiles. Indeed, since this pioneering work, a large PAH IR spectroscopic database has emerged summarizing results from both calculations and extensive experimental IR studies of (large) PAHs and their cations either isolated in the gas phase or embedded in a matrix [e.g. 8–14].

Further studies have revealed that the spectroscopic properties as well as the dissociation characteristics of PAHs are highly dependent on structure, size and particularly symmetry and edge topology [14–19]. The more symmetric pericondenced PAHs may be more photostable and exhibit bands that best resemble the resolved class A and B type bands as classified by Peeters et al. [20]. The irregular (catacondensed) PAH species, on the other hand, are thought to be less photostable [15,16]. They furthermore do not exhibit resolved IR bands that are condensed by degeneracy, but more dense spectra with IR activity covering wavelengths corresponding with the class C and D type spectra [14]. It has been suggested that only the very symmetric and most photostable PAHs can survive the harsh radiation conditions in many astronomical environments and this would be in line with species giving rise to the sharp and well-defined IR bands observed towards class A and B type sources. The irregular and less symmetric PAHs, on the other hand, can only survive in regions with much weaker radiation fields and get photodepleted or converted into more symmetric and stable species. This picture of photoprocessing of PAHs to the most stable species is known as the GrandPAH hypothesis [21].

* Corresponding author.
E-mail address: bouwman@strw.leidenuniv.nl (J. Bouwman).
URL: https://home.strw.leidenuniv.nl/bouwman/ (J. Bouwman).

https://doi.org/10.1016/j.jms.2021.111458
0022-2852/© 2021 The Authors. Published by Elsevier Inc.
This is an open access article under the CC BY license (http://creativecommons.org/licenses/by/4.0/).

In this study, we present the IR spectroscopic investigation of three structural isomers of $C_{24}H_{14}$ composition, namely dibenzo [a,h]pyrene (DBPah, C_{2h} symmetry), di-benzo[a,e]pyrene (DBPae, C_s symmetry), and di-benzo[a,l]pyrene (DBPal, C_1 symmetry) (See Fig. 1 for the chemical structures). These species are interesting subjects for study as they are PAH species with the same elemental composition, yet belonging to three different point groups. The latter is expected to have large bearings on both their IR spectroscopic appearance and photostability, as will be discussed here. The manuscript is organized as follows. The experimental technique and computational method are described first, after which the results are presented and discussed. Lastly, the data are put in light of earlier findings by Schlemmer et al. [5] and (astronomically relevant) conclusions are drawn.

2. Methods

2.1. Experimental

The experiments have been conducted on our instrument for Photodynamics of PAHs (iPoP) connected to the free electron laser for infrared experiments (FELIX) at Radboud University. The experimental setup and the used methodology have been described in much detail in previous publications [13,14,22,23] and a detailed description of FELIX is also available from the literature [24]. In this work, we only provide a description of the overall procedure and the relevant details.

The experimental system consists of a Paul-type quadrupole ion trap (QIT) that is connected to a reflectron time-of-flight (re-TOF) mass spectrometer. The QIT is mounted inside of a high-vacuum system that is pumped down by a turbomolecular pump to a pressure lower than 10^{-8} mbar. Helium is admitted to the ion trap assembly through a leak valve resulting in a pressure of 5×10^{-6} mbar during operation of the ion trap. The addition of helium to the ion trap helps to reduce the size of the ion cloud, resulting in a better mass resolution, and increases the ionization efficiency of the PAH species under investigation. The re-TOF tube is pumped by a separate turbopump resulting in a pressure better than 10^{-8} mbar while helium is being admitted to the ion trap.

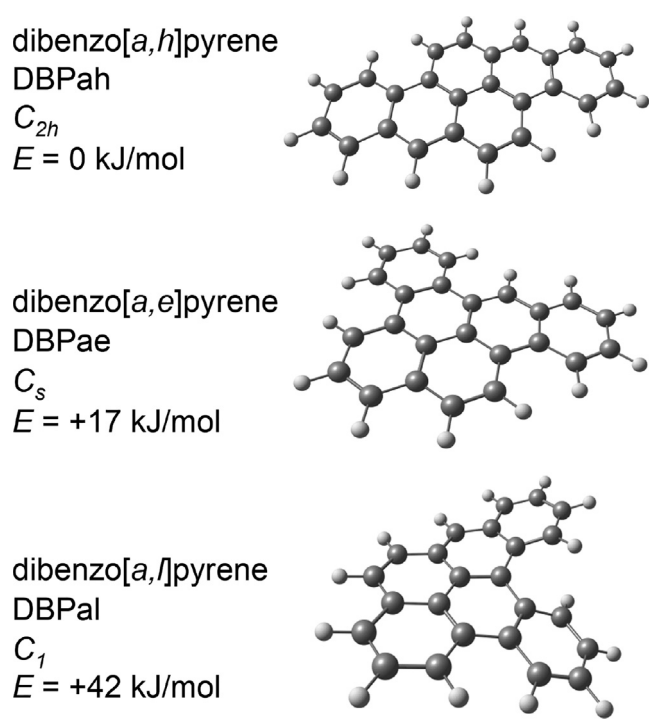

Fig. 1. Molecular structures of the three $C_{24}H_{14}$ dibenzopyrene isomers discussed in this work listed together with their abbreviated names, their point groups and the relative energies calculated at the B3LYP/6-311++G** level.

The three dibenzopyrene samples are used as commercially available from Chiron (DBPah 99,8%, DBPae 99,5%, and DBPal 99,5%). The species of interest is placed in a ceramic oven that is temperature controlled by means of a K-type thermocouple and a PID controller. The oven is situated in the main vacuum chamber just outside of the QIT assembly at the repeller side of the QIT. The dibenzopyrene isomer is evaporated very gently at a temperature of about 135 °C and subsequently ionized by collisions with 80 eV electrons that are emitted from the hot filament of an electron gun that is placed next to the oven's exit. The formed PAH cations are steered into the ion trap through a hole in the back of the repeller endcap of the QIT by means of a set of three electrostatic lenses. Ions are only admitted into the ion trap for a fill time set to 1.2 s. After the fill time has passed, the ion gate is set high and ions are deflected, thereby prohibiting them from entering the trap. Once in the QIT, the ions are trapped in the radiofrequency (1 MHz) field of 2200 $V_{top-top}$ that is applied to the ring electrode of the QIT. The ions are subsequently isolated by applying a 140 ms long Stored Waveform Inverse Fourier Transform (SWIFT) pulse composed following the method described by Doroshenko and Cotter [25]. The SWIFT pulse filters out all fragment ions formed by electron ionization as well as other contaminants, while retaining the $m/z = 302$ ions that correspond to the PAH cation of interest. In order to rule out any isomeric pollution, the isomers are measured sequentially and the oven was cleaned and baked out at a temperature exceeding 250 °C prior to measuring a new species.

Next, the mass-filtered ions are exposed to the intense IR radiation emitted from FELIX. The IR light is focused onto the ion cloud by a concave gold mirror that is placed in a nitrogen-purged box outside of the experimental chamber. The IR laser light enters the experimental system through a KBr window that acts as the vacuum seal. The radiation from FELIX is tuned over the 600–1800 cm^{-1} wavenumber range and has pulse intensities that reach around 180 mJ per pulse at its peak power. FELIX is operated at a repetition rate of 10 Hz and each emitted macropulse is about 8 μs long and consists of a train of micropulses. The ion cloud is exposed to two IR macropulses and the ions in the trap get efficiently dissociated when resonantly excited. In the range from 1100 to 1700 cm^{-1} the parent DBPah and DBPal ions are found to dissociate fully upon being exposed to two laser pulses and therefore scans are also performed with a single IR laser pulse and the laser power attenuated by 3 dB. The spectrum of the DBPae cation has only been measured at an attenuation of 5 dB to stay well away from saturation of absorption bands.

The remaining parent ion as well as fragment ions that form after being exposed to mid-IR radiation are ejected out of the QIT and into the re-TOF mass spectrometer. Ions are detected onto a Z-gap configuration microchannel plate detector and the signal is recorded using a time-binning data acquisition card. The frequency is scanned from 1800 to 600 cm^{-1} in steps of 3 cm^{-1} and two mass spectra are averaged to give a measurement at each laser frequency. The spectrum is constructed from the dissociation yield as a function of wavenumber as is described in Section 3.2. FELIX provides radiation with a bandwidth of approximately ~ 5 cm^{-1}. However, the IRMPD method inherently results in absorption bands that are broadened, resulting in a typical Full-Width-at-Half-Maximum (FWHM) of ~ 30 cm^{-1}.

2.2. Computational

DFT is employed to compute vibrational normal modes of the three studied PAH cations and to this end, we use the Gaussian16

quantum chemical software package [26]. Molecular structures are optimized at the B3LYP/ 6-311++G** level of theory and the resulting vibrational normal modes are energy scaled by applying a uniform scaling factor of 0.965 [27]. The resulting stick spectrum is subsequently convolved with a Gaussian shape with a FWHM of 30 cm^{-1} to allow for comparison with the experimental data.

3. Results and discussion

The mid-IR spectra of the three DBP isomers have been investigated by means of IRMPD spectroscopy. First the mass spectrometric results are presented, followed by IR spectra that are constructed from the wavelength-dependent mass spectra.

3.1. Mass spectrometry

Fig. 2 shows the resulting mass spectra for the three DBP isomers. From the top spectra (shown in black) it is clear that the SWIFT method cleanly isolates the parent ion and only very small leftover contributions of fragment ions that form upon dissociative electron ionization are apparent. Isomerization of the DBP species upon electron ionization cannot be fully ruled out, but is expected to play a minor role. Molecules with sufficient energy to overcome typical barriers for isomerization are expected to dissociate rather than to equilibrate elsewhere on the potential energy surface. This is in line with previous work on naphthalene by Solano and Mayer [28], who showed that the energy barrier for isomerization is close to the energy required for dissociation via H loss or C_2H_2 loss. Moreover, a full kinetic treatment led them to conclude that isomerization and subsequent stabilization of the isomer is unlikely.

The trapped and isolated DBP parent ions are subsequently exposed to the focused radiation from the free electron laser. Dissociation is induced when the frequency of the IR radiation is tuned into resonance with a vibrational normal mode of the molecular ion. This is apparent from the mass spectra that have been recorded after the ions were excited, as can be seen in the bottom panels of Fig. 2. These mass spectra have been extracted for each of the isomers at a frequency that corresponds to the maximum dissociation of the parent ion. A train of mass peaks is visible that corresponds to the successive loss of hydrogen atoms with a very distinct pattern that points to the loss of an even number of hydrogen atoms being dominant, as is commonly observed in the photodissociation of PAHs [29]. In some cases, particularly for the DBPah and DBPae isomer, signals corresponding to the loss of C_2 or C_2H_2 are also apparent. The parent ion is still clearly visible, indicating that the signal does not saturate. In this work, the dissociation signals are used for recording the IR action spectra only (see next section). The underlying dissociation characteristics of the three isomers will be subject of a future study.

3.2. Mid-IR spectroscopy

Mid-IR action spectra of the three DBP isomers are extracted from the TOF mass spectra recorded as a function of laser wavelength. To this end, the IRMPD fragment yield (η) is determined from the mass spectra for each of the IR excitation wavelengths according to:

$$\eta = \frac{\int \text{frag}}{(\int \text{par} + \int \text{frag})}, \tag{1}$$

where frag and par indicate the fragment and parent ion signals, respectively. The integrated values of the parent and dissociation fragment ion signals are retrieved from a Pearson IV fitting procedure applied to the TOF signals as observed in Fig. 2. Subsequently, the fragment yield at each IR frequency is corrected for the frequency dependent power emanating from the free electron laser, resulting in the spectra observed in Fig. 3. The top and bottom pannel of this figure contain both the spectrum recorded without laser power attenuation (0 dB, shown in black) as well as the spectrum recorded at 3 dB attenuation (dark gray). The middle pannel displays the spectrum recorded at 5 dB laser attenuation. The computed spectra are shown in blue for comparison.

The resulting IR spectra of all three species exhibit resolved and isolated vibrational modes in the 600–1000 cm^{-1} range and a series of vibrational bands stretching 1100–1650 cm^{-1}. All DBP isomers exhibit strong IR activity in this range and this becomes even more clear when looking at the DFT computed vibrational normal modes that are also displayed in Fig. 3. The vibrational modes are scaled by a uniform scaling factor of 0.965 and displayed as sticks. The spectral profile that results from convolving the stick spectrum with a Gaussian profile with a FWHM of 30 cm^{-1} is also shown. Although the experimental bands above 1100 cm^{-1} appear to be rather unresolved, a comparison of the measured IR spectrum with the computed IR spectrum clearly

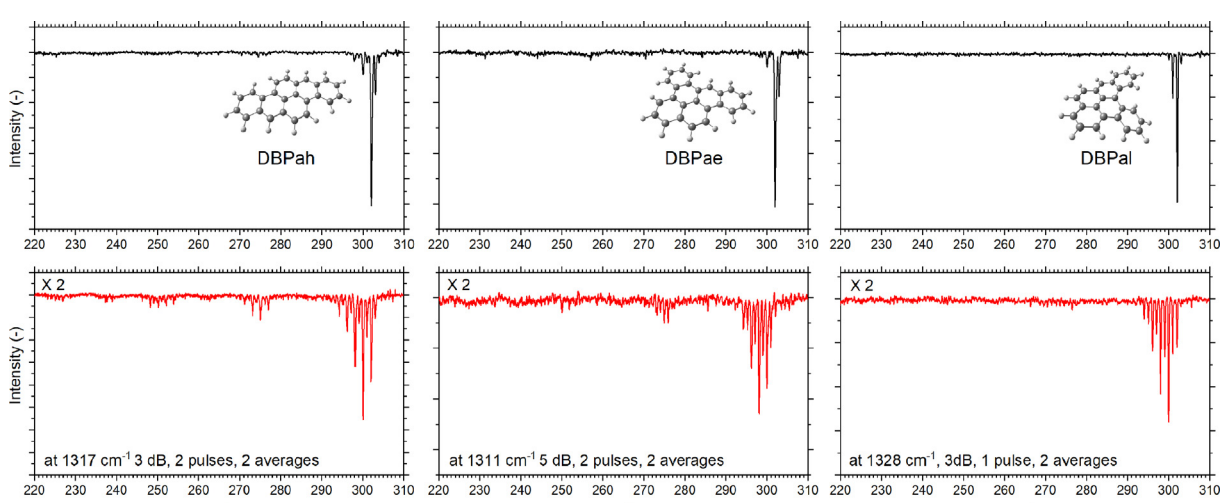

Fig. 2. Mass spectra of the three DBP isomers after non-resonant IR excitation (top) and after resonant excitation (bottom). Resonant excitations are performed at a frequency corresponding to the maximum absorption and using significant attenuation of the laser power (see labels) to ensure that the parent signal is not fully depleted.

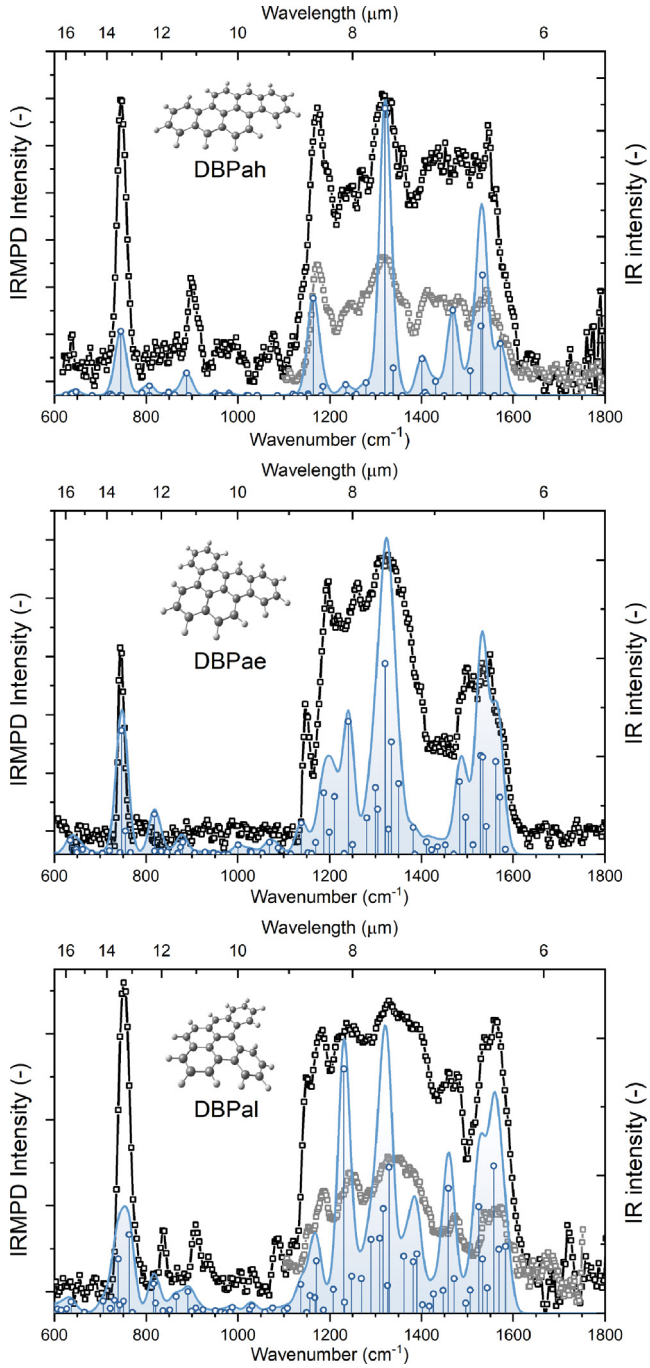

Fig. 3. IR spectra of the three DBP isomers as constructed from their IR frequency dependent dissociation mass spectra. The spectra recorded using unattenuated (black) as well as 3 dB attenuated (grey) laser radiation are shown in the top and bottom panel. The spectrum in the middle panel has been obtained at an attenuation of 5 dB. The sticks and line shown in blue represent the computed vibrational normal modes and the spectrum resulting from a convolution of these with a 30 cm^{-1} broad Gaussian profile, respectively.

Table 1
DBPah: Experimentally measured band positions for DBPah shown together with the computed IR intensity, symmetry label and difference between experimental and computed band position.

Experimental	Calculated[a,b]			
Pos. (cm^{-1})	Pos. (cm^{-1})	Int. (km/mol)	Sym.	$\Delta_{pos.}$ cm^{-1}
747	745	121	A_u	2
900	888	43	A_u	12
1166	1164	184	B_u	2
1199	...	...	...	...
1238	1235	20	B_u	4
1278	1279	24	B_u	-1
1317	1320	543	B_u	-3
1357	1338	52	B_u	19
1401	1401	69	A_g	0
1438	1431	27	B_u	8
1476	1468	161	B_u	8
1511	1506	47	B_u	5
...	1529	131	A_g	...
1547	1533	227	B_u	14
1584	1572	98	B_u	13

[a] The computed band positions are scaled with a factor of 0.965 to account for anharmonicities.
[b] Only modes with intensities ⩾ 20 km/mol are listed.

Table 2
DBPae: Experimentally measured band positions for DBPae shown together with the computed IR intensity, symmetry label and difference between experimental and computed band position.

Experimental	Calculated[a,b]			
Pos. (cm^{-1})	Pos. (cm^{-1})	Int. (km/mol)	Sym.	$\Delta_{pos.}$ cm^{-1}
746	746	126	A″	0
...	818	41	A′	
1150	1138	32	A′	11
1193	1187	63	A′	6
...	1199	23	A′	
1225	1211	59	A′	15
1257	1241	136	A′	16
1287	1281	38	A′	6
1313	1300	68	A′	13
...	1305	46	A′	
...	1321	195	A′	
...	1328	26	A′	
1342	1335	115	A′	7
1371	1350	73	A′	21
1400	1382	27	A′	17
1432	...	...	...	
1464	...	...	...	
1500	1483	74	A′	17
...	1496	38	A′	
1539	1529	101	A′	10
...	1534	99	A′	
...	1541	28	A′	
1573	1562	95	A′	11
...	1571	59	A′	

[a] The computed band positions are scaled with a factor of 0.965 to account for anharmonicities.
[b] Only modes with intensities ⩾ 20 km/mol are listed.

shows that many bands are quite well reproduced in terms of their peak position. In terms of intensity, however, there is a clear mismatch between the experimental and computed spectra as is commonly observed for IRMPD spectra.

Gaussian line profile fits were made to the experimental data to allow for further comparison between the experimental and computational bands. Peak positions and integrated intensities were left as free parameters and an upper limit of 30 cm^{-1} was given to the FWHM to match the experimental data. Prior to starting the fit procedure, peaks were defined manually at positions where a clear peak or wing was observed in the experimental spectrum, i.e. fully unbiased by the computed positions of the vibrational bands. The resulting global fit and individual Gaussian profiles are shown in Appendix A of this manuscript.

The peak positions resulting from the Gaussian fits are summarized in Tables 1–3. Also shown in these tables are the positions of the DFT computed vibrational bands scaled to account for anharmonicities, the intensity of the band, and the symmetry of the

Table 3
DBPal: Experimentally measured band positions for DBPal shown together with the computed IR intensity, symmetry label and difference between experimental and computed band position.

Experimental	Calculated[a,b]			
Pos. (cm^{-1})	Pos. (cm^{-1})	Int. (km/mol)	Sym.	$\Delta_{pos.}$ cm^{-1}
751	739	39	A	11
768	763	57	A	5
837	816	21	A	21
911	...	...	...	...
1151	1137	21	A	14
1183	1171	38	A	12
1218	1231	178	A	-13
1248	1248	27	A	1
1279	1269	25	A	10
...	1290	54	A	...
1308	1309	54	A	-1
...	1317	76	A	...
...	1326	20	A	...
1335	1329	106	A	6
1366	1361	41	A	4
...	1382	37	A	...
1397	1390	43	A	7
1428	...	...	...	...
1456	1459	91	A	-3
1482	1471	25	A	11
1509	1525	77	A	-16
1533	1533	39	A	0
...	1543	18	A	...
1566	1557	107	A	9
...	1569	46	A	...
1596	1583	49	A	13

[a] The computed band positions are scaled with a factor of 0.965 to account for anharmonicities.
[b] Only modes with intensities ⩾ 20 km/mol are listed.

mode. Only theoretical band positions with calculated IR intensities exceeding 20 km/mol are listed in the tables. It is interesting to note here that the DBPal isomer is in fact a chiral molecule, but that this is obviously not reflected in the IR spectra, where no distinction between the two stereo isomers can be made.

The experimentally measured (fitted) band positions are matched in the table to the computed band that lies closest in frequency. The last column of the table displays the difference between the experimental (fitted) band position and the computed (scaled) value. Generally, there is a reasonable match between the computed and fitted band positions and only in a few cases the shift between the fit and the computed band is larger than 15 cm^{-1}. The peak positions for the DBPae isomer show the largest deviations, which is caused by the fairly unstructured spectrum that made it hard to find initial fit parameters. For all isomers, a few of the detected experimental bands do not have a corresponding computed band. This is caused by the fact that small computed bands with low intensities (i.e. not listed in the table) add up to give an observable experimental band. Other effects such as the non-linear laser power response of IRMPD may also cause some bands to show up stronger than predicted by computations. In a few other cases, computed bands with significant intensity have no experimental counterpart. This is a result of the applied methodology where fit parameters were selected by an unbiased visual inspection of the experimental data, rather than guided by the computed peak positions.

4. Conclusion

The work presented here connects beautifully to the sophisticated pioneering studies performed by Schlemmer et al. [5], who were the first to report laboratory measured IR bands emitted from

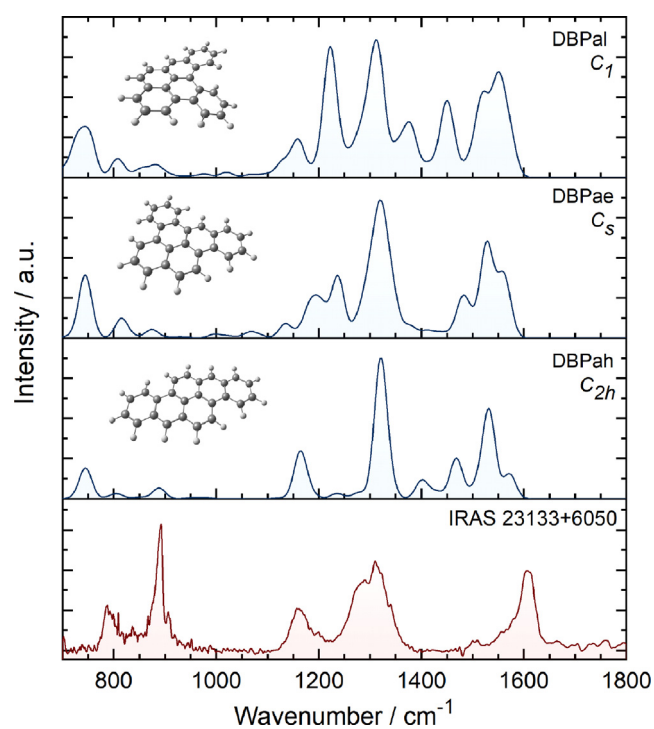

Fig. 4. The Class A type IR emission spectrum as seen towards IRAS 23133+6050 from *ISO*/SWS [30,31] calibrated by Sloan et al. [32] (in red) compared with the simulated IR spectra of the three isomeric PAH species discussed in this work (in blue). (For interpretation of the references to color in this figure legend, the reader is referred to the web version of this article.)

hot UV excited neutral PAHs. From this study, they concluded that the IR bands are likely caused by larger PAHs and PAH cations and that small PAHs do not contribute significantly. The mass spectrometric data hint to small and irregular molecules being highly susceptible to decomposition by breaking down the carbon skeleton, as is apparent from the ease with which these molecules dissociated in our experiments and the high laser attenuation needed to not fully dissociate our parent cations. This is very different from pericondensed PAHs, for example the $C_{24}H_{12}$ molecule coronene, that has a comparable size and appears to be much more resilient to breaking down of the carbon backbone [19].

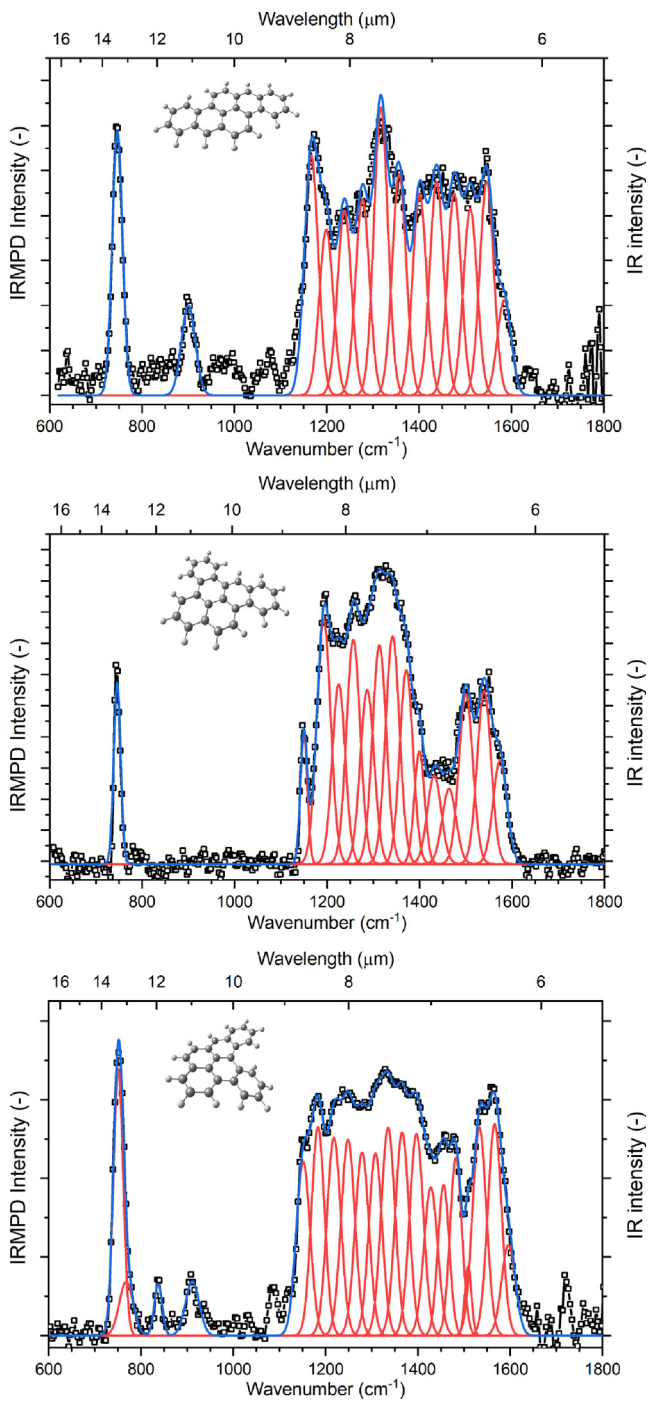

Fig. 5. IR spectra of the three DBP isomers (black) shown together with the multi component Gaussian fit (blue) as well as the individual Gaussian components (red). (For interpretation of the references to color in this figure legend, the reader is referred to the web version of this article.)

Our findings further show that the IR spectra of the lower symmetry PAHs of $C_{24}H_{14}$ composition, i.e. the species with the highest relative energy (see Fig. 1), exhibit denser IR spectra that do not match the typical isolated and well-defined IR emission bands seen towards many interstellar objects. This is exemplified in Fig. 4, where the class A type IR emission spectrum observed towards the photodissociation region associated with IRAS 23133 + 6050 [30,31] is compared with the computed and convolved IR (absorption) spectra of our three studied DBP isomers. From this comparison it is clear that, although the absolute positions of the bands do not match, the appearance of isolated bands in the observational data matches best with the DBP isomer of highest symmetry. The molecules with lower symmetry, on the other hand, have enhanced IR activity that contradicts the observational data. Hence, this work lends credit to the GrandPAH hypothesis that suggests that small and irregular PAHs are more efficiently photodissociated in heavily irradiated regions in space, leaving behind only a subset of remaining chemically stable and highly symmetric molecules that give rise to the sharp IR emission features.

CRediT authorship contribution statement

Jordy Bouwman: Conceptualization, Formal analysis, Funding acquisition, Investigation, Methodology, Writing – original draft. **Harold Linnartz:** Funding acquisition, Methodology, Resources, Writing – reviewing & editing. **Alexander G.G.M. Tielens:** Conceptualization, Methodology, Writing - review & editing.

Declaration of Competing Interest

The authors declare that they have no known competing financial interests or personal relationships that could have appeared to influence the work reported in this paper.

Acknowledgement

JB acknowledges the Netherlands Organisation for Scientific Research (Nederlandse Organisatie voor Wetenschappelijk Onderzoek, NWO) for a Vidi grant (Grant No. 723.016.006) which was used to support this work. This work was carried out on the Dutch national e-infrastructure with the support of SURF Cooperative (46011). The authors acknowledge the European Union (EU) and Horizon 2020 funding awarded under the Marie Skłodowska-Curie action to the EUROPAH consortium (Grant No. 722346). The authors gratefully thank the staff at FELIX Laboratory for their local support.

Appendix A

The results of the Gaussian fit procedure are presented in Fig. 5. These fits are made by initially selecting peak positions in an unbiased manner and subsequently allowing for free fitting of the measured spectra. Only the upper limit of the Gaussian profiles FWHM was restricted and set to 30 cm^{-1} to resemble the experimental data. Individual Gaussian profiles are shown in red, while the overall fit to the experimental data is shown in blue.

References

[1] A. Leger, J.L. Puget, Identification of the unidentified IR emission features of interstellar dust, A&A 137 (1) (1984) L5–L8.
[2] L.J. Allamandola, A.G.G.M. Tielens, J.R. Barker, Polycyclic aromatic hydrocarbons and the unidentified infrared emission bands: auto exhaust along the Milky Way, ApJ 290 (1) (1985) L25–L28, https://doi.org/10.1086/184435.

[3] A.G.G.M. Tielens, Interstellar polycyclic aromatic hydrocarbon molecules, ARA&A 46 (2008) 289–337, https://doi.org/10.1146/annurev.astro.46.060407.145211.
[4] L.J. Allamandola, A.G.G.M. Tielens, J.R. Barker, Interstellar polycyclic aromatic hydrocarbons - The infrared emission bands, the excitation/emission mechanism, and the astrophysical implications, ApJS 71 (1989) 733–775, https://doi.org/10.1086/191396.
[5] S. Schlemmer, D.J. Cook, J.A. Harrison, B. Wurfel, W. Chapman, R.J. Saykally, The unidentified interstellar infrared bands: PAHs as carriers?, Science 265 (5179) (1994) 1686–1689, https://doi.org/10.1126/science.11539830. https://science.sciencemag.org/content/265/5179/1686. ISSN 0036-8075.
[6] D.J. Cook, S. Schlemmer, N. Balucani, D.R. Wagner, B. Steiner, R.J. Saykally, Infrared emission spectra of candidate interstellar aromatic molecules, Nature 380 (6571) (1996) 227–229, https://doi.org/10.1038/380227a0.
[7] D.J. Cook, S. Schlemmer, N. Balucani, D.R. Wagner, J.A. Harrison, B. Steiner, R.J. Saykally, Single photon infrared emission spectroscopy: A study of IR emission from UV laser excited PAHs between 3 and 15 μm, J. Phys. Chem. A 102 (9) (1998) 1465–1481, https://doi.org/10.1021/jp9724434. ISSN 1089-5639.
[8] M. Vala, J. Szczepanski, F. Pauzat, O. Parisel, D. Talbi, Y. Ellinger, Electronic and vibrational spectra of matrix-isolated pyrene radical cations: Theoretical and experimental aspects, J. Phys. Chem 98 (37) (1994) 9187–9196, https://doi.org/10.1021/j100088a017.
[9] C. Joblin, L. D'Hendecourt, A. Leger, D. Defourneau, Infrared spectroscopy of gas-phase PAH molecules. 1: Role of the physical environment, A&A 281 (1994) 923–936.
[10] Jos Oomens, Gerard Meijer, Gert von Helden, Gas phase infrared spectroscopy of cationic indane, acenaphthene, fluorene, and fluoranthene, J. Phys. Chem. A 105 (36) (2001) 8302–8309, https://doi.org/10.1021/jp0110455.
[11] C.W. Bauschlicher Jr., C. Boersma, A. Ricca, A.L. Mattioda, J. Cami, E. Peeters, F. Sánchez de Armas, G. Puerta Saborido, D.M. Hudgins, L.J. Allamandola, The NASA Ames polycyclic aromatic hydrocarbon infrared spectroscopic database: The computed spectra, ApJS 189 (2) (2010) 341–351, https://doi.org/10.1088/0067-0049/189/2/341.
[12] C. Boersma, C.W. Bauschlicher Jr., A. Ricca, A.L. Mattioda, J. Cami, E. Peeters, F. Sánchez de Armas, G. Puerta Saborido, D.M. Hudgins, L.J. Allamandola, The NASA Ames PAH IR spectroscopic database version 2.00: Content, web site, and on(off)line tools, ApJS 211 (1) (2014) 8, https://doi.org/10.1088/0067-0049/211/1/8.
[13] J. Zhen, P. Castellanos, J. Bouwman, H. Linnartz, A.G.G.M. Tielens, Infrared spectra of hexa-peri-hexabenzocoronene cations: HBC^{+} and HBC^{2+}, ApJ 836 (2017) 28, https://doi.org/10.3847/1538-4357/836/1/28.
[14] J. Bouwman, P. Castellanos, M. Bulak, J. Terwisscha van Scheltinga, J. Cami, H. Linnartz, A.G.G.M. Tielens, Effect of molecular structure on the infrared signatures of astronomically relevant PAHs, A&A 621 (2019) A80, https://doi.org/10.1051/0004-6361/201834130.
[15] S.P. Ekern, A.G. Marshall, J. Szczepanski, M. Vala, Photodissociation of gas-phase polycylic aromatic hydrocarbon cations, J. Phys. Chem. A 102 (20) (1998) 3498–3504.
[16] H.W. Jochims, H. Baumgartel, S. Leach, Structure-dependent photostability of polycyclic aromatic hydrocarbon cations: Laboratory studies and astrophysical implications, ApJ 512 (1) (1999) 500–510, https://doi.org/10.1086/306752.
[17] J. Bouwman, A.J. de Haas, J. Oomens, Spectroscopic evidence for the formation of pentalene^{+} in the dissociative ionization of naphthalene, Chem. Commun. 52 (2016) 2636–2638, https://doi.org/10.1039/C5CC10090A.
[18] A.J. de Haas, J. Oomens, J. Bouwman, Facile pentagon formation in the dissociation of polyaromatics, PCCP 19 (2017) 2974–2980, https://doi.org/10.1039/C6CP08349H.
[19] S. Panchagnula, J. Bouwman, D.B. Rap, P. Castellanos, A. Candian, C. Mackie, S. Banhatti, S. Brünken, H. Linnartz, A.G.G.M. Tielens, Structural investigation of doubly-dehydrogenated pyrene cations, PCCP 22 (2020) 21651–21663, https://doi.org/10.1039/D0CP02272A.
[20] E. Peeters, S. Hony, C. Van Kerckhoven, A.G.G.M. Tielens, L.J. Allamandola, D.M. Hudgins, C.W. Bauschlicher, The rich 6 to 9 μm spectrum of interstellar PAHs, A&A 390 (2002) 1089–1113, https://doi.org/10.1051/0004-6361:20020773.
[21] H. Andrews, C. Boersma, M.W. Werner, J. Livingston, L.J. Allamandola, A.G.G.M. Tielens, PAH Emission at the Bright Locations of PDRs: the grandPAH Hypothesis, ApJ 807 (2015) 99, https://doi.org/10.1088/0004-637X/807/1/99.
[22] J. Zhen, D.M. Paardekooper, A. Candian, H. Linnartz, A.G.G.M. Tielens, Quadrupole ion trap/time-of-flight photo-fragmentation spectrometry of the hexa-peri-hexabenzocoronene (HBC) cation, CPL 592 (2014) 211–216, https://doi.org/10.1016/j.cplett.2013.12.005.
[23] J. Bouwman, C. Boersma, M. Bulak, J. Kamer, P. Castellanos, A.G.G.M. Tielens, H. Linnartz, Gas-phase infrared spectroscopy of the rubicene cation ($c_{26}h_{14}^{+}$) - A case study for interstellar pentagons, A&A 636 (2020) A57, https://doi.org/10.1051/0004-6361/201937013.
[24] D. Oepts, A.F.G. van der Meer, P.W. van Amersfoort, The free-electron-laser user facility FELIX, Infrared Phys. Technol. 36 (1) (1995) 297–308, https://doi.org/10.1016/1350-4495(94)00074-U.
[25] V.M. Doroshenko, R.J. Cotter, Advanced stored waveform inverse fourier transform technique for a matrix-assisted laser desorption/ionization quadrupole ion trap mass spectrometer, Rapid Commun. Mass Spectrometry 10 (1) (1996) 65–73.
[26] M.J. Frisch, G.W. Trucks, H.B. Schlegel, G.E. Scuseria, M.A. Robb, J.R. Cheeseman, G. Scalmani, V. Barone, G.A. Petersson, H. Nakatsuji, X. Li, M. Caricato, A.V. Marenich, J. Bloino, B.G. Janesko, R. Gomperts, B. Mennucci, H.P. Hratchian, J.V. Ortiz, A.F. Izmaylov, J.L. Sonnenberg, D. Williams-Young, F. Ding, F. Lipparini, F. Egidi, J. Goings, B. Peng, A. Petrone, T. Henderson, D. Ranasinghe, V.G. Zakrzewski, J. Gao, N. Rega, G. Zheng, W. Liang, M. Hada, M. Ehara, K. Toyota, R. Fukuda, J. Hasegawa, M. Ishida, T. Nakajima, Y. Honda, O. Kitao, H. Nakai, T. Vreven, K. Throssell, J.A. Montgomery, Jr., J.E. Peralta, F. Ogliaro, M.J. Bearpark, J.J. Heyd, E.N. Brothers, K.N. Kudin, V.N. Staroverov, T.A. Keith, R. Kobayashi, J. Normand, K. Raghavachari, A.P. Rendell, J.C. Burant, S.S. Iyengar, J. Tomasi, M. Cossi, J.M. Millam, M. Klene, C. Adamo, R. Cammi, J.W. Ochterski, R. L. Martin, K. Morokuma, O. Farkas, J.B. Foresman, D.J. Fox, Gaussian1~6 Revision C.01, 2016. Gaussian Inc., Wallingford CT.
[27] M.P. Andersson, P. Uvdal, New scale factors for harmonic vibrational frequencies using the B3LYP density functional method with the triple-ζbasis set 6–311+G(d, p), J. Phys. Chem. A 109 (12) (2005) 2937–2941, https://doi.org/10.1021/jp045733a.
[28] E.A. Solano, P.M. Mayer, A complete map of the ion chemistry of the naphthalene radical cation? DFT and RRKM modeling of a complex potential energy surface, J. Chem. Phys. 143 (10) (2015) 104305, https://doi.org/10.1063/1.4930000.
[29] P. Castellanos, A. Candian, J. Zhen, H. Linnartz, A.G.G.M. Tielens, Photoinduced polycyclic aromatic hydrocarbon dehydrogenation the competition between H- and H_2-loss, A&A 616 (2018) A166, https://doi.org/10.1051/0004-6361/201833220.
[30] M.F. Kessler, J.A. Steinz, M.E. Anderegg, J. Clavel, G. Drechsel, P. Estaria, J. Faelker, J.R. Riedinger, A. Robson, B.G. Taylor, S. Ximénez de Ferrán, The Infrared Space Observatory (ISO) mission, A&A 315 (1996) L27–L31.
[31] T. de Graauw, L.N. Haser, D.A. Beintema, P.R. Roelfsema, H. van Agthoven, L. Barl, O.H. Bauer, H.E.G. Bekenkamp, A.-J. Boonstra, D.R. Boxhoorn, J. Cote, P. de Groene, C. van Dijkhuizen, S. Drapatz, J. Evers, H. Feuchtgruber, M. Frericks, R. Genzel, G. Haerendel, A.M. Heras, K.A. van der Hucht, T. van der Hulst, R. Huygen, H. Jacobs, G. Jakob, T. Kamperman, R.O. Katterloher, D.J.M. Kester, D. Kunze, D. Kussendrager, F. Lahuis, H.J.G.L.M. Lamers, K. Leech, S. van der Lei, R. van der Linden, W. Luinge, D. Lutz, F. Melzner, P.W. Morris, D. van Nguyen, G. Ploeger, S. Price, A. Salama, S.G. Schaeidt, N. Sijm, C. Smoorenburg, J. Spakman, H. Spoon, M. Steinmayer, J. Stoecker, E.A. Valentijn, B. Vandenbussche, H. Visser, C. Waelkens, L.B.F.M. Waters, J. Wensink, P.R. Wesselius, E. Wiezorrek, E. Wieprecht, J.J. Wijnbergen, K.J. Wildeman, E. Young, Observing with the ISO Short-Wavelength Spectrometer, A&A 315 (1996) L49–L54.
[32] G.C. Sloan, K.E. Kraemer, S.D. Price, R.F. Shipman, A Uniform Database of 2.4-45.4 Micron Spectra from the Infrared Space Observatory Short Wavelength Spectrometer, ApJS 147 (2003) 379–401, https://doi.org/10.1086/375443.